

***Ab initio* angle- and energy-resolved photoelectron spectroscopy with time-dependent density-functional theory**U. De Giovannini,^{1,*} D. Varsano,² M. A. L. Marques,³ H. Appel,⁴ E. K. U. Gross,⁵ and A. Rubio¹¹*University of the Basque Country UPV/EHU, Nano-Bio Spectroscopy Group, Avenida de Tolosa 72, 20018 San Sebastian, Spain*²*Department of Physics, University of Rome “La Sapienza,” Piazzale Aldo Moro 5, 00185 Roma, Italy*³*Université de Lyon, F-69000 Lyon, France and LPMC, CNRS, UMR 5586, Université Lyon 1, F-69622 Villeurbanne, France*⁴*Fritz-Haber-Institut der Max-Planck-Gesellschaft, Faradayweg 4-6, D-14195 Berlin, Germany*⁵*Max-Planck Institute for Microstructure Physics, Weinberg 2, 06120 Halle, Germany*

(Received 1 June 2012; published 27 June 2012)

We present a time-dependent density-functional method able to describe the photoelectron spectrum of atoms and molecules when excited by laser pulses. This computationally feasible scheme is based on a geometrical partitioning that efficiently gives access to photoelectron spectroscopy in time-dependent density-functional calculations. By using a geometrical approach, we provide a simple description of momentum-resolved photoemission including multiphoton effects. The approach is validated by comparison with results in the literature and exact calculations. Furthermore, we present numerical photoelectron angular distributions for randomly oriented nitrogen molecules in a short near-infrared intense laser pulse and helium-(I) angular spectra for aligned carbon monoxide and benzene.

DOI: [10.1103/PhysRevA.85.062515](https://doi.org/10.1103/PhysRevA.85.062515)

PACS number(s): 31.15.E–, 33.60.+q, 33.80.Eh, 33.80.Rv

I. INTRODUCTION

Photoelectron spectroscopy is a widely used technique to analyze the electronic structure of complex systems [1,2]. The advent of intense ultrashort laser sources has extended the range of applicability of this technique to a vast variety of nonlinear phenomena like high-harmonic generation, above-threshold ionization (ATI), bond softening, and vibrational population trapping [3]. Furthermore, it turned attosecond time-resolved pump-probe photoelectron spectroscopy into a powerful technique for the characterization of excited-states dynamics in nanostructures and biological systems [4]. Angular-resolved ultraviolet photoelectron spectroscopy is by now established as a powerful technique for studying geometrical and electronic properties of organic thin films [5,6]. Time-resolved information from streaking spectrograms [7], shearing interferograms [8], photoelectron diffraction [9], photoelectron holography [10], etc. hold the promise of wave function reconstruction together with the ability to follow the ultrafast dynamics of electronic wave packets. Clearly, to complement all these experimental advances, and to help to interpret and understand the wealth of new data, there is the need for *ab initio* theories able to provide (time-resolved) photoelectron spectra (PES) and photoelectron angular distributions (PAD) for increasingly complex atomic and molecular systems subject to arbitrary perturbations (laser intensity and shape).

Photoelectron spectroscopy is a general term which refers to all experimental techniques based on the photoelectric effect. In photoemission experiments a light beam is focused on a sample, transferring energy to the electrons. For low light intensities an electron can absorb a single photon and escape from the sample with a maximum kinetic energy $\hbar\omega - I_P$ (where ω is the photon angular frequency and I_P the first

ionization potential of the system), while for high intensities electron dynamics can be interpreted considering a three-step model [11]. This model provides a semiclassical picture in terms of ionization followed by free electron propagation in the laser field with return to the parent ion, and rescattering. Such rescattering processes are the source of many interesting physical phenomena. In the case of long pulses, for instance, multiple photons can be absorbed resulting in emerging kinetic energies of $s\hbar\omega - I_P - U_P$ (where s is the number of photons absorbed, $U_P = \epsilon^2/4\omega^2$ is the ponderomotive energy, and ϵ the electric field amplitude) forming the so-called ATI peaks in the resulting photoelectron spectrum. In all cases the observable is the escaping electron momentum measured at the detector.

In general, the interaction between electrons in an atom or molecule and a laser field is difficult to treat theoretically, and several approximations are usually performed. Clearly, a full many-body description of PES is prohibitive, except for the case of few (one or two) electron systems [12–14]. As a consequence, the direct solution of the time-dependent Schrödinger equation (TDSE) in the so-called single-active electron (SAE) approximation is a standard investigation tool for many strong-field effects in atoms and dimers and represents the benchmark for analytic and semianalytic models [7,10,15–26]. Perturbative approaches based on the standard Fermi golden rule are usually employed. For weak lasers, plane wave methods [5] and the independent atomic center approximation [27] have been applied, while in the strong-field regime, Floquet theory, the strong-field approximation [10,28], and semiclassical methods [11,29,30] are routinely used.

From a numerical point of view, it would be highly desirable to have a PES theory based on time-dependent density-functional theory (TDDFT) [31,32] where the complex many-body problem is described in terms of a fictitious single-electron system. For a given initial many-body state, TDDFT maps the whole many-body problem into the time dependence of the density from which all physical properties can be obtained. The method is in principle exact, but in practice

*umberto.degiovannini@ehu.es

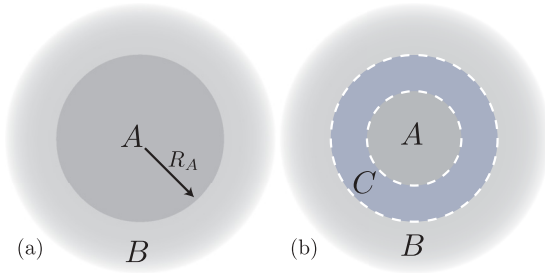


FIG. 1. (Color online) Schematic description of (a) the partitioning of space for the phase space method and (b) the mask method. Region A is the interaction region, B is the Volkov propagation region, and C is the overlap region where Ψ_A and Ψ_B mix under the mask function.

approximations have to be made for the unknown exchange-correlation functional as well as for specific density functionals providing physical observables. This latter issue is much less studied than the former. In any case, several works were published addressing the problem of single and multiple ionization processes within TDDFT. For example, ionization rates were calculated for atoms and molecules [33–37], and TDDFT with the sampling point method (SPM) has been employed in the study of PES and PAD for sodium clusters [38–41].

In this work, besides presenting a formal derivation of a photoelectron orbital functional, we report on a physically sound scheme to compute PES of interacting electronic systems in terms of the time-dependent single electron Kohn-Sham (KS) wave functions. The scheme relies on geometrical considerations and is based on a splitting technique [16–20]. The idea is based on the partitioning of space in two regions (see Fig. 1): in the inner region, the KS wave function is obtained by solving the TDDFT equations numerically; in the outer region, electrons are considered as free particles, the Coulomb interaction is neglected, and the wave function is propagated analytically with only the laser field. Electrons flowing from the inner region to the outer region are recorded and coherently summed up to give the final result. In addition to the adaptation of the traditional splitting procedure to TDDFT, we propose a scheme where electrons can seamlessly drift from one region to the other and spurious reflections are greatly suppressed. This procedure allows us to reduce considerably the spatial extent of the simulation box without damaging the accuracy of the method.

The rest of this paper is organized as follows. The formalism for describing photoelectrons in TDDFT is delineated in Sec. II. In order to make contact with the literature, we first give a brief introduction to the state-of-the-art for the *ab initio* calculation of PES for atomic and molecular systems. In Sec. II A we introduce the geometrical approach in the context of quantum phase space. The phase-space approach is then derived in the case of effective single-particle theories like TDDFT in Sec. II B. In Sec. II C we introduce the mask method, an efficient propagation scheme based on space partitioning.

Three applications of the mask method are presented in Sec. III. One application deals with the hydrogen atom and illustrates the different mask methods in a simple one-dimensional model also in comparison with the sampling point method [38]. The above threshold ionization of

three-dimensional hydrogen is examined and compared with values from the literature. In the second application we illustrate PADs from randomly oriented nitrogen molecules in a strong near-infrared ultrashort laser pulse. Comparison with the experiment and molecular strong-field approximation is discussed [28]. The third application of the method regards helium-(I) (wavelength 58 nm) PADs for oriented carbon monoxide and benzene. Results are discussed in comparison with the plane wave approximation. Finally, in Sec. IV we discuss the results and present the conclusions.

All our numerical calculations were performed with the real-time, real-space TDDFT code OCTOPUS [42,43], freely available under the GNU public license. Atomic units are used throughout unless otherwise indicated.

II. MODELING PHOTOELECTRON SPECTRA

In order to put in perspective the results of the present paper, we will give a brief introduction on the status of the principal techniques available for *ab initio* PES calculations. We start our description with the methods employed to study one-electron systems.

For one-electron systems PES can be calculated exactly from the direct solution of the TDSE. Several methods have been employed to extract PES information from the solution of the TDSE. The most direct and intuitive way is via direct projection methods where the PES is obtained by projecting the wave function at the end of the pulse onto the eigenstates describing the continuum. These eigenstates are extracted through the direct diagonalization of the Hamiltonian without including the interaction with the field. The momentum probability distribution can then be easily obtained from the Fourier transform of the continuum part of the time-dependent wave function [23].

Another approach, that avoids the calculation of the full continuum spectrum, involves the analysis of the exact wave function $|\Psi\rangle$ after the laser pulse via a resolvent technique [15,26]. In this case, the energy-resolved PES is given by the direct projection on outgoing wave functions with $P(E) = |\langle\Phi(E)|\Psi\rangle|^2 = \langle\Psi|\hat{D}(E)|\Psi\rangle$, where $\Phi(E)$ denotes an outgoing (unbound) electron of energy E of the laser-free Hamiltonian, and $\hat{D}(E)$ is the corresponding projection operator that can be conveniently approximated [15,26].

Normally, one needs accurate wave functions in a large space domain to obtain the correct distribution of the ejected electrons. This is because the unbound parts of the wave packet spread out of the core region, and conventional expressions for the transition amplitude need these parts of the wave function. Solving the TDSE within all the required volume in space can easily become a very difficult computational problem. Several techniques were developed during the years to solve the problem. For simple cases these difficulties can be overcome by the use of spherical coordinates. Geometrical splitting techniques have also been employed [16–20]. Furthermore, formulations in the Kramers-Henneberger frame of reference [44] and in momentum space [24] led to calculations with remarkable high precision. Recently, a promising surface flux method has also been proposed [25].

The exact solution of the TDSE in three dimensions for more than two electrons is unfeasible and the limit rises to

four electrons for one-dimensional models [45]. Due to this limitation basically all *ab initio* calculations for multielectron systems are performed under the SAE approximation. In the SAE only one electron interacts with the external field while the other electrons are frozen [21], and the TDSE is thus solved only for the active electron. This approximation has been successfully employed in several photoemission studies for atoms and molecules in strong laser fields [7,10,22]. However, the failure of this simple model to describe multielectron (correlation) effects calls for better schemes [22].

The inclusion of exchange-correlation effects for a system of many interacting electrons can be achieved within TDDFT while keeping the simplicity of working with a set of time-dependent (fictitious) single-particle orbitals. In spite of transferring all the many-body problems into an unknown exchange-correlation functional, the lack of a density functional providing the electron emission probability is a major limitation for a direct access to photoelectron observables from the time evolution of the density (note that, in spite of the Runge-Gross theorem [31] stating that all observables are functionals of the time-dependent density, in practice we know few observables that can be written in terms of the time-dependent density, one example being the absorption spectra).

There have been some attempts to describe PES and multiple ionization processes with TDDFT in the standard adiabatic approximation [33–37]. All these works use boundary absorbers to separate the bound and continuum part of the many-body wave function. The emission probability is then correlated with the time dependence of the number of bound electrons.

An alternative and simple scheme is provided by the SPM [38]. Here the idea is to record single-particle wave functions in time at a fixed sampling point r_S away from the core. The time Fourier transform of the wave function recorded at r_S represents the probability of having an electron in r_S with energy E . The probability to detect one electron with energy E in r_S is then given by the sum over all occupied orbitals:

$$P_{r_S}(E) = \sum_{i=1}^{\text{occ}} |\psi_i(\mathbf{r}_S, E)|^2. \quad (1)$$

This method is easy to implement, can be extended to give also angular information [41], and is also clearly applicable to the TDSE in the SAE. However, it lacks formal derivation as it is directly based on Kohn-Sham wave functions without a direct connection to the many-body state. Furthermore, it is strongly dependent on the position of the sampling point and the minimum distance. This distance sometimes turns out to be quite large in order to avoid artifacts, and is strongly dependent on the laser pulse properties. We discuss further details concerning this method in Sec. III A.

In the following, we present an alternative method inspired by geometrical splitting and derive it from a phase-space point of view. The method can be naturally converged by increasing the size of the different simulation boxes.

A. Phase-space geometrical interpretation

An intuitive description of photoelectron experiments can be obtained resorting to a phase-space picture. Experimental

detectors are able to measure photoelectron velocity with a certain angular distribution for a sequence of ionization processes with similar initial conditions. The quantity available at the detector is therefore connected to the probability to register an electron with a given momentum \mathbf{p} at a certain position \mathbf{r} . From this consideration it would be tempting to interpret photoemission experiments with a joint probability distribution in the phase space (\mathbf{r}, \mathbf{p}) . Such a classical picture, however, conflicts with the fundamental quantum mechanics notion of the impossibility to simultaneously measure momentum and position, and prevents us from proceeding in this direction. A link between the classical and quantum picture is needed beforehand.

In order to make a connection to a microscopic description it turns out to be convenient to extend the classical concept of phase-space distributions to the quantum realm. A common prescription comes from the Wigner transform of the one-body density matrix with respect to the center of mass $\mathbf{R} = (\mathbf{r} + \mathbf{r}')/2$ and relative $\mathbf{s} = \mathbf{r} - \mathbf{r}'$ coordinates. The d -dimensional (here and after $d \leq 3$) transform is defined as

$$w(\mathbf{R}, \mathbf{p}, t) = \int \frac{d\mathbf{s}}{(2\pi)^{\frac{d}{2}}} e^{i\mathbf{p}\cdot\mathbf{s}} \rho(\mathbf{R} + \mathbf{s}/2, \mathbf{R} - \mathbf{s}/2, t), \quad (2)$$

with

$$\begin{aligned} \rho(\mathbf{r}, \mathbf{r}', t) &= \int d\mathbf{r}_2 \dots d\mathbf{r}_N \Psi(\mathbf{r}, \mathbf{r}_2, \dots, \mathbf{r}_N, t) \\ &\times \Psi^*(\mathbf{r}', \mathbf{r}_2, \dots, \mathbf{r}_N, t), \end{aligned} \quad (3)$$

being the one-body density matrix, and $\Psi(\mathbf{r}_1, \mathbf{r}_2, \dots, \mathbf{r}_N, t)$ the N -body wave function of the system at time t . The Wigner function defined above is normalized and its integral over the whole space (momentum) gives the probability to find an electron with momentum \mathbf{p} (position \mathbf{R}). As the uncertainty principle prevents the simultaneous knowledge of position and momentum, $w(\mathbf{R}, \mathbf{p})$ cannot be a proper joint distribution. Moreover, it can assume negative values due to nonclassical dynamics. Nevertheless, the Wigner function $w(\mathbf{R}, \mathbf{p})$ constitutes a concept close to a probability distribution in phase space (\mathbf{R}, \mathbf{p}) compatible with quantum mechanics.

The quantum phase space naturally leads to a geometrical interpretation of photoemission. One could think to divide the space in two regions A and B as in Fig. 1(a), where region B represents the region where detectors are positioned and A is defined as the complement of B . In this picture, PES can be seen as the probability to have an electron with given momentum in B . It is then natural to define the momentum-resolved photoelectron spectrum as

$$\mathcal{P}(\mathbf{p}) = \lim_{t \rightarrow \infty} \int_B d\mathbf{R} w(\mathbf{R}, \mathbf{p}, t), \quad (4)$$

where the spatial integration is carried out in region B , and the limit $t \rightarrow \infty$ assures that region B contains all photoelectron contributions. From the knowledge of the momentum-resolved PES [cf. Eq. (4)] one can access several different quantities by simple integration. For instance, in three dimensions ($d = 3$) the energy-resolved PES is obtained integrating over the solid angle Ω :

$$P(E = p^2/2) = \int_0^{4\pi} d\Omega \mathcal{P}(\mathbf{p}), \quad (5)$$

and the photoelectron angular distribution in the system reference frame is given by

$$P(E = p^2/2, \theta) = \int_0^{2\pi} d\phi \mathcal{P}(\mathbf{p}). \quad (6)$$

In spite of giving an intuitive picture of PES, Eq. (4) is not suited for direct numerical evaluation since it requires the knowledge of the full one-body density matrix in the whole space. In the next section we will make a contact with effective single-particle theories like TDDFT to overcome the limitations due to the knowledge of the many-body wave function. In order to avoid integration over the whole space an efficient evolution scheme is presented in Sec. II C.

B. Phase-space interpretation within TDDFT

TDDFT is an effective-single particle theory where the many-body wave function is described by an auxiliary single Slater determinant $\Psi_{\text{KS}}(\mathbf{r}_1, \dots, \mathbf{r}_N)$ built out of Kohn-Sham orbitals $\psi_i(\mathbf{r})$ [31,32]. In order to simplify the notation, we drop the explicit time dependence from the wave functions and assume that the following equations are written in the limit $t \rightarrow \infty$ as prescribed by Eq. (4).

Being represented by a single determinant, the one-body Kohn-Sham density matrix is given by

$$\rho_{\text{KS}}(\mathbf{r}, \mathbf{r}') = \sum_{i=1}^{\text{occ}} \psi_i(\mathbf{r}) \psi_i(\mathbf{r}'), \quad (7)$$

where the sum is carried out over all occupied orbitals. Performing a decomposition of each orbital according to the partition of Fig. 1(a) we obtain

$$\psi_i(\mathbf{r}) = \psi_{A,i}(\mathbf{r}) + \psi_{B,i}(\mathbf{r}), \quad (8)$$

where $\psi_{A,i}(\mathbf{r})$ is the part of the wave function describing states localized in A and $\psi_{B,i}(\mathbf{r})$ is the ionized contribution measured at the detector in B . The one-body density matrix can now be accordingly decomposed as a sum of four terms:

$$\rho_{\text{KS}}(\mathbf{r}, \mathbf{r}') = \sum_{i=1}^{\text{occ}} [\psi_{A,i}(\mathbf{r}) \psi_{A,i}^*(\mathbf{r}') + \psi_{A,i}(\mathbf{r}) \psi_{B,i}^*(\mathbf{r}') + \psi_{B,i}(\mathbf{r}) \psi_{A,i}^*(\mathbf{r}') + \psi_{B,i}(\mathbf{r}) \psi_{B,i}^*(\mathbf{r}')]. \quad (9)$$

From Eq. (9) we can build the KS Wigner function defined in Eq. (2) and obtain the momentum-resolved probability distribution by inserting it into Eq. (4). We note that this step involves a nontrivial approximation, namely that the KS one-body density matrix is a good approximation to the fully interacting one in region B . This is, however, much milder than the assumption that the Kohn-Sham determinant is a good approximation to the many-body wave function in region B , as it is done, e.g., in the SPM.

The final result is a sum of four overlap double integrals that can be simplified further. For a detailed calculation we refer to Appendix A. The first overlap integral, containing a product of two functions localized in A [cf. Eq. (9)], is zero due to the spatial integration in B . The two next overlap integrals, containing mixed products of wave functions localized in A and B , can be reduced by increasing the size of region A . Assuming A to be large enough to render these terms negligible

the only integral we are left with is the one containing functions in B , leading to

$$\mathcal{P}(\mathbf{p}) \approx \int_B d\mathbf{R} \int \frac{d\mathbf{s}}{(2\pi)^d} e^{i\mathbf{p}\cdot\mathbf{s}} \sum_{i=1}^{\text{occ}} \psi_{B,i}\left(\mathbf{R} + \frac{\mathbf{s}}{2}\right) \psi_{B,i}^*\left(\mathbf{R} - \frac{\mathbf{s}}{2}\right). \quad (10)$$

The approximation sign \approx is a reminder for the error committed in discarding the mixed overlap integrals. Since the probability of finding an ionized electron in region A is zero for $t \rightarrow \infty$, we can extend the integration over B in Eq. (10) to the whole space. Using the integral properties of the Wigner transform, we finally obtain

$$\mathcal{P}(\mathbf{p}) \approx \sum_{i=1}^{\text{occ}} |\tilde{\psi}_{B,i}(\mathbf{p})|^2, \quad (11)$$

where $\tilde{\psi}_{B,i}(\mathbf{p})$ is the Fourier transform of $\psi_{B,i}(\mathbf{r})$ and the expression is written in the limit for $t \rightarrow \infty$. Equation (11) gives an intuitive formulation of momentum-resolved PES as a sum of the Fourier component of each orbital in the detector region. It is worth noting that Eq. (11) is not restricted to TDDFT and can be applied to other effective single-particle formulations such as time-dependent Hartree-Fock and the TDSE in the SAE approximation.

The numerical evaluation of the ionization probability from Eq. (11) requires the knowledge of the wave function after the external field has been switched off. For ionization processes this means that one has to deal with simulation boxes that extend over several hundred atomic units and this practically constrains the method only to one-dimensional calculations. In the next section we will derive a simple scheme to overcome this limitation making the present scheme applicable for realistic simulations of molecules and nanostructures.

C. The mask method

In the previous sections we described a practical way to evaluate the momentum-resolved PES following the spatial partitioning of Fig. 1(a) and how this can be conveniently cast in the language of TDDFT. In this section we take a step further in developing an efficient time evolution scheme by exploiting the geometry of the problem together with some physical assumptions.

We start by introducing a split-evolution scheme. At each time t we implement a spatial partitioning of Eq. (8) as follows:

$$\begin{cases} \psi_{A,i}(\mathbf{r}, t) = M(\mathbf{r}) \psi_i(\mathbf{r}, t), \\ \psi_{B,i}(\mathbf{r}, t) = [1 - M(\mathbf{r})] \psi_i(\mathbf{r}, t), \end{cases} \quad (12)$$

where $M(\mathbf{r})$ is a smooth mask function defined to be 1 deep in the interior of region A and 0 outside, as shown in Fig. 2. Such a mask function, along with the partitions A and B , introduces a buffer region C (technically handled as the outermost shell of A), where $\psi_{A,i}(\mathbf{r}, t)$ and $\psi_{B,i}(\mathbf{r}, t)$ overlap [see Fig. 1(b)].

We can set up a propagation scheme from time t to t' as follows:

$$\begin{cases} \psi_{A,i}(\mathbf{r}, t') = M(\mathbf{r}) U(t', t) [\psi_{A,i}(\mathbf{r}, t) + \psi_{B,i}(\mathbf{r}, t)], \\ \psi_{B,i}(\mathbf{r}, t') = [1 - M(\mathbf{r})] U(t', t) [\psi_{A,i}(\mathbf{r}, t) + \psi_{B,i}(\mathbf{r}, t)], \end{cases} \quad (13)$$

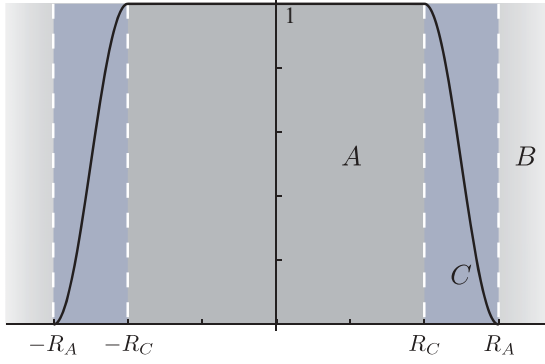


FIG. 2. (Color online) Mask function implements a smooth transition from region A to region B. The functional shape used for actual calculations is defined in Eq. (18).

where $U(t',t)$ is the time propagator associated with the full Hamiltonian including the external fields. Equation (13) defines a recursive propagation scheme completely equivalent to a time propagation in the whole space $A \cup B$.

In typical experimental setups, detectors are situated far away from the sample and electrons overcoming the ionization barrier travel a long way before being detected. During their journey toward the detector, and far away from the molecular system, they practically evolve as free particles driven by an external field. It seems therefore a waste of resources to solve the full Schrödinger equation for the traveling electrons while their behavior can be described analytically. In addition, an ideal detector placed relatively close to the molecular region would measure the same PES.

From these observations we conclude that we can reduce region A to the size of the interaction region and assume electrons in B to be well described by noninteracting Volkov states. Volkov states are the exact solution of the Schrödinger equation for free electrons in an oscillating field. They are plane waves and are therefore naturally described in momentum space. In the velocity gauge the Volkov time propagator is formally expressed by

$$U_V(t',t) = \exp \left\{ -i \int_t^{t'} d\tau \frac{1}{2} \left[\mathbf{p} - \frac{\mathbf{A}(\tau)}{c} \right]^2 \right\}, \quad (14)$$

where the time-ordering operator is omitted for brevity and $\mathbf{A}(\tau)$ is the vector potential. This is equivalent to the use of a strong-field approximation in the outer region in the same spirit of the Lewenstein model [46].

In summary, the method we propose consists in solving numerically the real-space TDDFT equations in A and analytically propagating the wave functions residing in B in momentum space. In this setup region C acts as a communication layer between functions in A and B. Under this prescription, and by handling B functions in momentum space, Eq. (13) becomes

$$\begin{cases} \psi_{A,i}(\mathbf{r},t') = \eta_{A,i}(\mathbf{r},t') + \eta_{B,i}(\mathbf{r},t'), \\ \tilde{\psi}_{B,i}(\mathbf{p},t') = \tilde{\xi}_{A,i}(\mathbf{p},t') + \tilde{\xi}_{B,i}(\mathbf{p},t'), \end{cases} \quad (15)$$

with

$$\eta_{A,i}(\mathbf{r},t') = M(\mathbf{r})U(t',t)\psi_{A,i}(\mathbf{r},t), \quad (16a)$$

$$\eta_{B,i}(\mathbf{r},t') = M(\mathbf{r}) \int \frac{d\mathbf{p}}{(2\pi)^{\frac{d}{2}}} e^{i\mathbf{p}\cdot\mathbf{r}} U_V(t',t) \tilde{\psi}_{B,i}(\mathbf{p},t), \quad (16b)$$

$$\tilde{\xi}_{A,i}(\mathbf{p},t') = \int \frac{d\mathbf{r}}{(2\pi)^{\frac{d}{2}}} e^{-i\mathbf{p}\cdot\mathbf{r}} [1 - M(\mathbf{r})] U(t',t) \psi_{A,i}(\mathbf{r},t), \quad (16c)$$

$$\tilde{\xi}_{B,i}(\mathbf{p},t') = U_V(t',t) \tilde{\psi}_{B,i}(\mathbf{p},t) - \int \frac{d\mathbf{r}}{(2\pi)^{\frac{d}{2}}} e^{-i\mathbf{p}\cdot\mathbf{r}} \eta_{B,i}(\mathbf{r},t'). \quad (16d)$$

At each time step the orbital $\psi_{A,i}$ is evolved under the mask function and stored in $\eta_{A,i}$, forcing $\eta_{A,i}$ to be localized in A. At the same time, the components of $\psi_{A,i}$ escaping from A are collected in momentum space by $\tilde{\xi}_{A,i}$. We then add to $\tilde{\xi}_{A,i}$ the contribution of the wave functions already present in B at time t by summing up $U_V \tilde{\psi}_{B,i}$. In order to allow electrons to come back from B to A we include $\eta_{B,i}$ in A and correct the function in B by removing its Fourier components [second term in Eq. (16d)].

One of the advantages of Eq. (15) is that all the spatial integrals present in $\eta_{B,i}(\mathbf{r},t')$ and $\tilde{\xi}_{B,i}(\mathbf{p},t')$ are performed on functions localized in C. Therefore, integrals over the whole space are evaluated at the cost of an integration on the much smaller buffer region C that can be easily evaluated by fast Fourier transform algorithms. Similar considerations hold for integrals in momentum space under the assumption that B functions $\tilde{\psi}_{B,i}(\mathbf{p},t)$ are localized in momentum. When region A is discretized on a grid, in order to avoid wave function wrapping at the boundaries and preserve numerical stability, additional care must be taken. In our implementation, numerical stability is addressed by the use of nonuniform Fourier transforms (see details in Appendix B).

There are situations where the electron flow from B to A is negligible. This is the case, for instance, when A is large enough to contain the whole wave functions at the time when the external field has been switched off. A propagation at later times will see photoelectrons flowing mainly from A to B. In this situation, $\eta_{B,i}$ and the corresponding correction term in $\tilde{\xi}_{B,i}$ can be discarded. The evolution scheme of Eq. (15) is thus simplified and becomes

$$\begin{cases} \psi_{A,i}(\mathbf{r},t') = \eta_{A,i}(\mathbf{r},t'), \\ \tilde{\psi}_{B,i}(\mathbf{p},t') = \tilde{\xi}_{A,i}(\mathbf{p},t') + U_V(t',t) \tilde{\psi}_{B,i}(\mathbf{p},t). \end{cases} \quad (17)$$

In the following we will refer to Eq. (17) as the “mask method”(MM), and to Eq. (15) as the “full mask method”(FMM). We note here again that, being single-particle propagations schemes, both MM and FMM are not restricted to TDDFT and can be applied to other effective single-particle theories. As a matter of fact, an approach similar to Eq. (17) has already been employed in the propagation of the TDSE equations for atomic systems [16,17,19], and in TDDFT for one-dimensional models of metal surfaces [47]. We also note that the implementation of absorbing boundaries through a mask function as done in Eq. (16a) can be cast in terms of an additional imaginary potential (exterior complex scaling) in the Schrödinger equation. Such an approach is commonly used in quantum optics.

Within MM, the evolution in A is completely unaffected by the wave functions in B and ionized electrons are treated

uniquely in momentum space. Compared with FMM, MM is numerically more stable as it is not affected by boundary wrapping. In order to achieve the conditions where Eq. (17) is valid may require, however, large simulation boxes. Moreover, as the mask function never absorbs perfectly the electrons, spurious reflections may appear. Suppression of such artifacts requires a further enlargement of the buffer region. With FMM spurious reflections are almost negligible.

Choosing between MM and FMM implies a tradeoff between computational complexity and numerical stability that strongly depends on the ionization dynamics of the process under study. In what follows, we will illustrate the differences and devise a prescription to help the choice of the most suitable method in each specific case.

III. APPLICATIONS

In this section we present a few numerical applications of the schemes previously derived. In all calculations the boundary between *A* and *B* regions is chosen as a *d*-dimensional sphere implemented by the mask function:

$$M(\mathbf{r}) = \begin{cases} 1 & \text{if } r < R_C, \\ 1 - \sin^2\left(\frac{(r-R_C)\pi}{2(R_A-R_C)}\right) & \text{if } R_C \leq r \leq R_A, \\ 0 & \text{if } r > R_A, \end{cases} \quad (18)$$

as shown in Fig. 2. Note that numerical studies (not presented here) revealed a weak dependence of the final results on the functional shape of the mask.

The time propagation of the orbitals in *A* is performed with the enforced time-reversal symmetry evolution operator [48]

$$U(t + \Delta t, t) = \exp\left(-i\frac{\Delta t}{2}H(t + \Delta t)\right) \exp\left(-i\frac{\Delta t}{2}H(t)\right), \quad (19)$$

where *H* is the full KS Hamiltonian, and the coupling with the external field is expressed in the velocity gauge.

The first system we will study is hydrogen. In spite of being a one-electron system, it is a seemingly trivial case that has been and still is under thorough theoretical investigation [23–25, 49–52]. Clearly, we do not need TDDFT to study hydrogen and our numerical results are obtained by propagating the wave function with a noninteracting Hamiltonian. The interest in this case is focused on the numerical performance of different mask methods as hydrogen provides a useful benchmark.

The full TDDFT calculations performed for molecular nitrogen, carbon monoxide, and benzene are later presented in Sec. III B and Sec. III C, respectively. In these cases, norm-conserving Troullier-Martins pseudopotentials and the exchange-correlation LB94 potential [53] (that has the correct asymptotic limit for molecular systems) are employed. Finally, in all calculations the starting electronic structure of the molecules is calculated in the Born-Oppenheimer approximation at the experimental equilibrium geometry and the time evolution is performed with fixed ions.

A. Photoelectron spectrum of hydrogen

As a first example we study multiphoton ionization of a one-dimensional soft-core hydrogen atom, initially in the ground

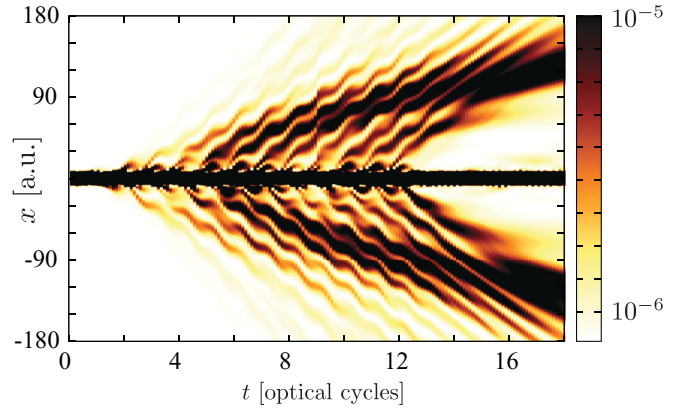


FIG. 3. (Color online) Evolution of the electronic density as a function of time $\rho(x, t) = |\psi(x, t)|^2$ for a one-dimensional soft-core hydrogen model. The laser pulse has angular frequency $\omega = 0.0856$ a.u., intensity $I = 1.38 \times 10^{13}$ W/cm², and a trapezoidal envelope with 2 optical cycle linear ramp (one optical cycle = 1.774 fs) and 10 cycles constant center.

state, and exposed to a $\lambda = 532$ nm ($\omega = 0.0856$ a.u.) linearly polarized laser pulse with peak intensity $I = 1.38 \times 10^{13}$ W/cm², of the form

$$A(t) = A_0 f(t) \cos(\omega t), \quad (20)$$

where $f(t)$ is a trapezoidal envelope function of 14 optical cycles with two-cycle linear ramps, constant for 10 cycles, and with $A_0 = 31.7$ a.u. Here $A(t)$ is the vector potential in units of the speed of light *c*. A soft-Coulomb potential $V(x) = -1/\sqrt{2+x^2}$ is employed to model the electron-ion interaction. We propagate the electronic wave function in time and then compare the energy-resolved ionization probability obtained from different schemes. Along with MM, FMM, and SPM we present results for direct evaluation of PES from Eq. (5). In this method the spectrum is obtained by directly Fourier transforming the wave function in region *B*. Since the analysis is conducted without perturbing the evolution of the wave function we will refer to it as the “passive method” (PM). This method requires the knowledge of the whole wave function after the pulse has been switched off, and since a considerable part of the wave packet is far away from the core (for the present case a box of 500 a.u. radius is needed for 18 optical cycles), it is viable only for one-dimensional calculations. Nevertheless, it is important as it constitutes the limiting case for both MM and FMM.

In Fig. 3, a color plot of the evolution of the electronic density as a function of time is shown. The electronic wave function splits into subpackets generated at each laser cycle (one optical cycle = $2\pi/\omega = 1.774$ fs). These wave packets evolve in bundles and their slope corresponds to a certain average momentum. ATI peaks are then formed by the buildup of interfering wave packets periodically emitted in the laser field and leading to a given final momentum [54].

From Fig. 3 it is possible to see that electrons may be considered as escaped “already” at 30 a.u. away from the center. We set therefore $R_A = 30$ a.u. and calculate energy-resolved PES with the PM. As we can see from Fig. 4 the spectrum presents several peaks at integer multiples of ω following $E = s\omega - I_p - U_p$ with $U_p = A_0^2/4c^2 = 0.0133$ a.u.

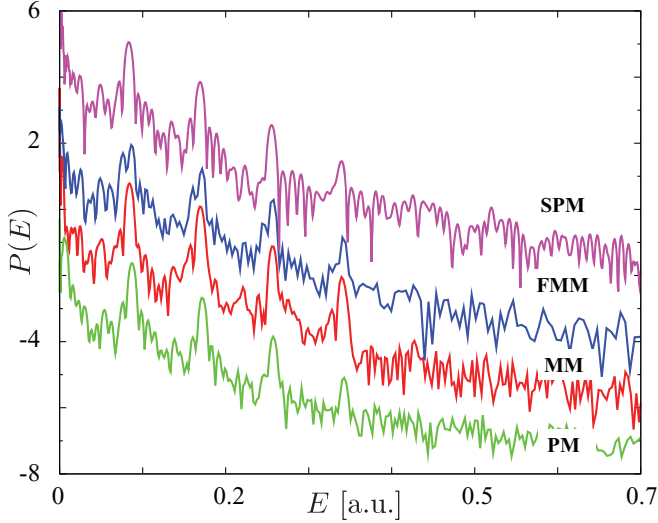


FIG. 4. (Color online) Energy-resolved photoelectron probability $P(E)$ (logarithmic scale) calculated with different approaches. The spectra are shifted by multiplying a constant factor for easy comparison. From bottom to top: passive method Eq. (5) in green, mask method Eq. (17) in red, full mask method Eq. (15) in blue, and sampling point method Eq. (1) in purple. Laser parameters are the same as in Fig. 3.

being the ponderomotive energy, $I_p = 0.5$ a.u. the ionization potential, and s the number of absorbed photons. In this case the minimum number of photons needed to exceed the ionization threshold is $s = 6$. Of course, the spectrum is only in qualitative agreement with three-dimensional calculations [15] as expected from a one-dimensional soft-core model [54–56].

PES calculated from MM, FMM, and SPM all agree as reported in Fig. 4. Numerical calculations were performed until convergence was achieved, leading to a grid with spacing $\Delta R = 0.4$ a.u. and box sizes depending on the method. For MM we employed a simulation box of $R_A = 70$ a.u. and set the buffer region at $R_C = 30$ a.u. In order to have energy resolution comparable with PM we used padding factors (see Appendix B) $P = P_N = 4$ and the total simulation time was $T = 18$ optical cycles. For FMM a smaller box of $R_A = 40$ a.u. with $R_C = 30$ a.u. is needed to converge results, and $P = 8$, $P_N = 2$ were needed to preserve numerical stability for $T = 18$ optical cycles. For SPM two sampling points at $r_S = -500, 500$ a.u. were needed to get converged results with a box of 550 a.u., and a complex absorber [57,58] at 49 a.u. from the boundaries of the box. In addition, a total time of $T = 74$ optical cycles was required to collect all the wave packets. The need for such a huge box resides on the working conditions of SPM. In order to avoid spurious effects, the sampling points must be set at a distance such that the density front arrives after the external field has been switched off. Therefore, the longer the pulse the further away the sampling points must be set. For these laser parameters one could rank each method according to increasing numerical cost starting from MM, followed by FMM, PM, and SPM.

As a second example we study the ionization of this one-dimensional hydrogen atom by an ultrashort intense infrared laser. We employ a single two-cycle pulse of wavelength $\lambda = 800$ nm ($\omega = 0.057$ a.u.), intensity $I = 2.5 \times 10^{14}$ W/cm²,

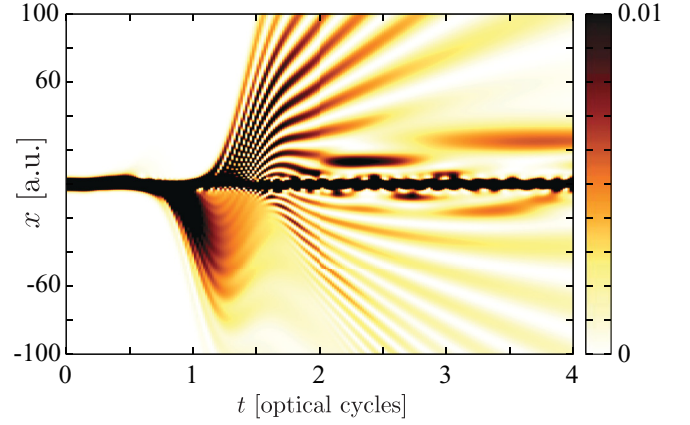


FIG. 5. (Color online) Density evolution $\rho(x,t)$ for a one-dimensional soft-core hydrogen and a two-cycle \sin^2 laser pulse with angular frequency $\omega = 0.057$ a.u., and intensity $I = 2.5 \times 10^{14}$ W/cm². Here one optical cycle = 2.66 fs.

and envelope

$$f(t) = \begin{cases} -\sin(\omega t/2N_c)^2 & \text{if } 0 \leq t \leq 2\pi N_c/\omega, \\ 0 & \text{if } t > 2\pi N_c/\omega, \end{cases} \quad (21)$$

with $N_c = 2$ and $A_0 = 225.8$ a.u.

Due to the laser strength and long wavelength, the electron evolution shown Fig. 5 is quite different from the one presented before. Electrons ejected from the core are driven by the laser and follow wide trajectories before returning to the parent ion. Such trajectories can be understood in the context of the semiclassical model [11] where released electrons move as a free particle in a time-dependent field with a maximum oscillation amplitude of $x_0 = 2A_0/\omega c = 57.8$ a.u. Electrons ejected near a maximum of the electric field $\epsilon(t) = -\partial A(t)/\partial t$ are the ones gaining the most kinetic energy and are therefore responsible for the fast emerging electrons after rescattering with the core.

In Fig. 6 we show the energy-resolved PES for different methods. Here the spectra appear to be very far from any ATI structure due to short duration of the laser pulse and is characterized by some irregular maxima and minima [23]. The characteristic features of the ionization dynamics is strongly dependent on the detailed shape of the pulse as one can easily imagine by inspecting the asymmetry in the electron ejection from Fig. 5. Due to these dynamics, a dramatic carrier envelope phase dependence for such short pulses is expected.

All the different methods result in similar spectra but with different parameters. In PM we set $R_A = 50$ a.u. and a box of radius $R = 700$ a.u. is needed to contain the wave function after $T = 4$ optical cycles (one optical cycle = 2.66 fs). For MM $R_A = 200$ a.u., $R_C = 40$ a.u., and the padding factors are $P = 2$, $P_N = 4$. Here the value for R_A is dictated by the width of the buffer region which needs to be wide enough to prevent spurious reflections. A considerably smaller box is needed for FMM, where $R_A = 60$ a.u., $R_C = 40$ a.u., $P = 4$, and $P_N = 2$. In this case one can reconstruct the total density in A by evaluating $|\psi_A(x,t)|^2$ via Eq. (15) and compare it to the exact evolution. As one can see in Fig. 7 the reconstructed density displays a behavior remarkably similar to the exact one of Fig. 5 but with a considerably reduced computational cost.

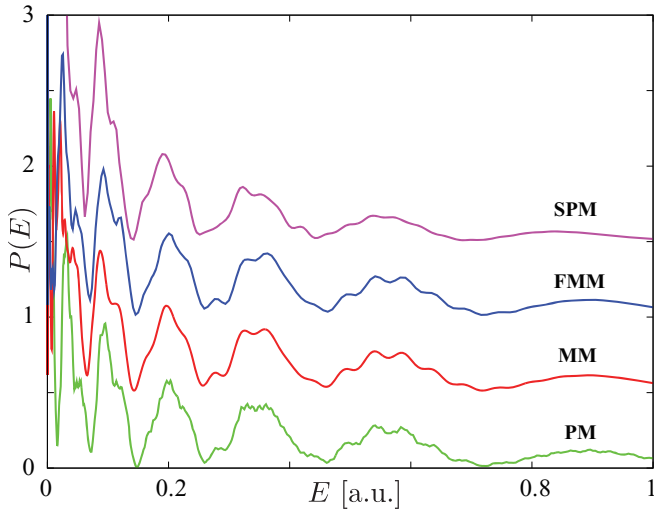


FIG. 6. (Color online) Energy-resolved photoelectron $P(E)$ yield from different approaches. Spectra are shifted by a constant factor. Order and color coding is the same as in Fig. 4. Laser parameters are described in the caption of Fig. 5.

SMP requires sampling points at $r_S = -130, 130$ a.u. in a box of radius $R = 200$ a.u. with 49 a.u. wide complex adsorbers, and for a total time of $T = 7$ optical cycles.

The possibility to use relatively small simulation boxes is especially important for three-dimensional calculations where the computational cost scales with the third power of the box size. Both mask methods are practicable options for three-dimensional simulations and the advantage of using FMM with respect to MM is driven by the electron dynamics. For long laser pulses MM appears to be more stable and it is a better choice than FMM, while for short pulses with large electron oscillations FMM can be more performant. SPM is a viable option for short pulses and small values for the oscillations.

As a last example, we present ATI of a real three-dimensional hydrogen atom subject to a long infrared pulse. We employ a laser linearly polarized along the x axis with wavelength $\lambda = 800$ nm, intensity $I = 5 \times 10^{13}$ W/cm², and pulse shape of the form (21) with $N_c = 20$ and $A_0 = 91.3$ a.u.

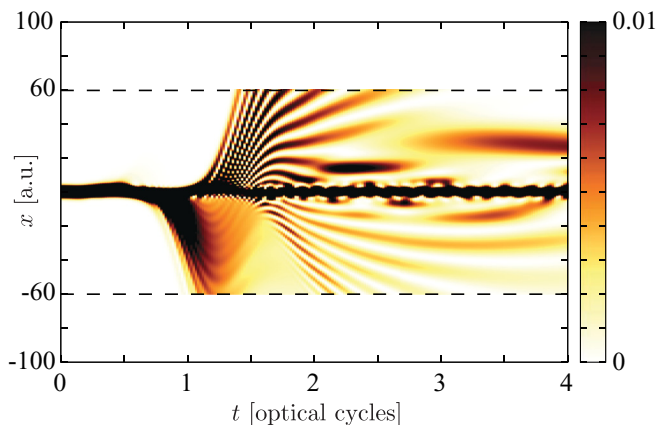


FIG. 7. (Color online) FMM density evolution $|\psi_A(x,t)|^2$ of a one-dimensional soft-core hydrogen. Laser parameters are the same as in Fig. 5. Dashed lines indicate the edges of the simulation box.

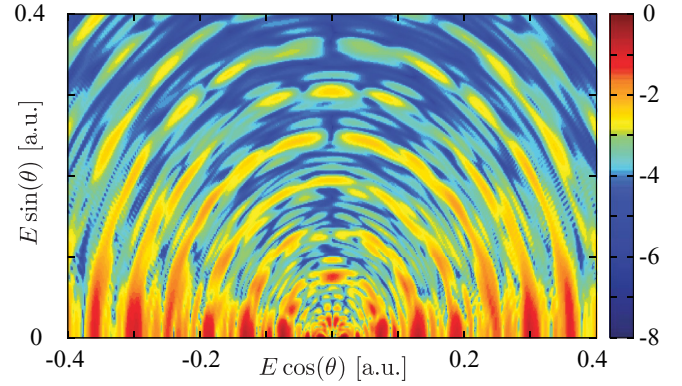


FIG. 8. (Color online) Photoelectron angular distribution $P(E,\theta)$ (logarithmic scale) of hydrogen for a 20 cycle \sin^2 laser pulse of wavelength $\lambda = 800$ nm, and intensity $I = 5 \times 10^{13}$ W/cm² polarized along the x axis.

Due to the pulse length, MM appears to be the most appropriate choice in this case. In the calculation $R_A = 60$ a.u., $R_C = 50$ a.u., $P = 1$, and $P_N = 8$.

In Fig. 8 we show a high-resolution density plot of the PAD $P(E,\theta)$ defined in Eq. (6). The radial distance denotes the photoelectron energy while the angle indicates the direction of emission with respect to the laser polarization. The color density is plotted in logarithmic scale and represents the values of $P(E,\theta)$.

The photoelectron energy-angular distribution displays complex interference patterns. The pattern shape compares favorably with similar calculations in the literature [24,25,44,59]. It consists of a series of rings with fine structures. Each ring represents the angular distribution of the photoelectron ATI peaks. The spacing of adjacent rings equals the photon energy $\omega = 0.057$ a.u. Photoelectrons are emitted mainly along the laser polarization, and the left-right symmetry of the rings indicates that the photoelectrons do not present any preferential ejection side with respect to the polarization axis. The first ring corresponds to the angular distribution of the first ATI peak. It presents a peculiar nodal pattern that is induced by the long-range Coulomb potential and is related to the fact that the ATI peak is determined by one dominant partial wave in the final state [60]. The number of the stripes equals the angular momentum quantum number of the dominant partial wave in the final state plus one [60]. In Fig. 8, the first ring contains six stripes and the dominant final state has angular momentum quantum number of 5. The pattern of the energy-angular distribution and the stripe number of the first ring are in good agreement with those in the literature [24,44]. As for the fine structures, we observe that while the main ring pattern is already formed in the first half of the pulse, the fine structure builds up until the end of the pulse. This supports the hypothesis that such structures are induced by the coherence of the two contributions from the leading and trailing edges of the pulse envelope [44].

B. N₂ under a few-cycle infrared laser pulse

In this section we compare theoretical and experimental angular resolved photoelectron probabilities for randomly oriented N₂ molecules. We choose the laser parameters

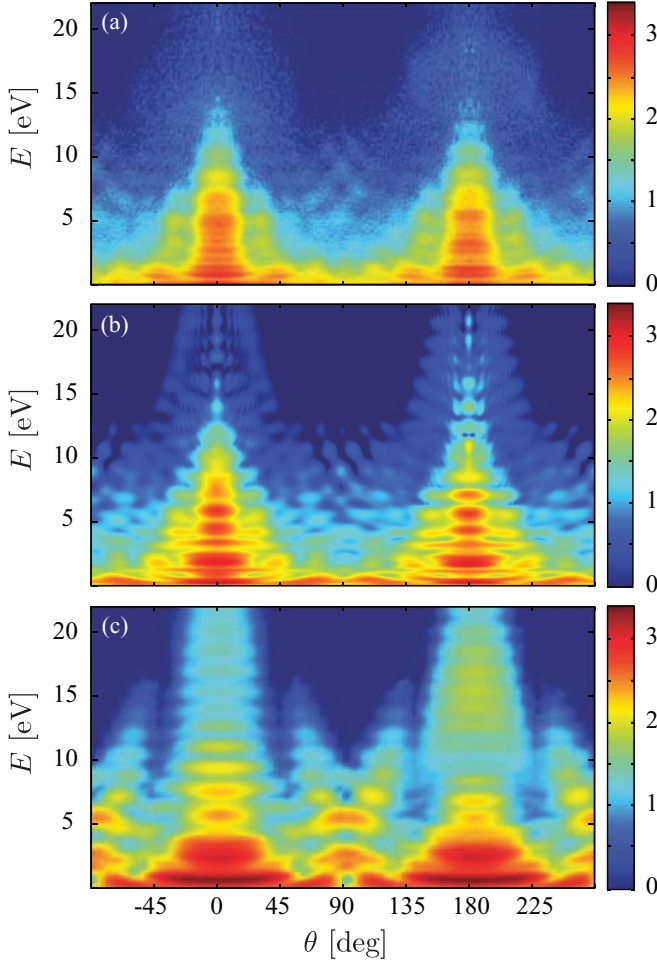


FIG. 9. (Color online) Photoelectron angle- and energy-resolved probability $\bar{P}(E, \theta)$ (log scale) in the laboratory frame for randomly oriented N_2 molecules in a 6 cycles infrared laser pulse with $\lambda = 750$ nm, with intensity $I = 4.3 \times 10^{13} \text{ W/cm}^2$. The angle θ is measured from the laser polarization axis. The different panels represent $\bar{P}(E, \theta)$ (spanning 3.4 orders of magnitude), from (a) experiment, (b) calculated with TDDFT and FMM, and (c) calculated with modified molecular strong-field approximation. Panels (a) and (c) are adapted from Ref. [28].

according to experiment [28], i.e., we employ a $N_c = 6$ cycle pulse of wavelength $\lambda = 750$ nm ($\omega = 0.06$ a.u.) and intensity $I = 4.3 \times 10^{13} \text{ W/cm}^2$. A laser shape

$$\mathbf{A}(t) = \begin{cases} \frac{A_0}{2} (1 - \cos(\frac{\omega t}{N_c})) \sin(\omega t) & \text{if } 0 \leq t \leq 2\pi N_c / \omega, \\ 0 & \text{if } t > 2\pi N_c / \omega \end{cases} \quad (22)$$

for the vector potential should lead to an electric field similar to the one employed in the experiment with zero carrier envelope phase.

In Fig. 9(a) the experimental photoelectron probability $\bar{P}(E, \theta)$ is plotted in logarithmic scale as a function of the energy and the angle with respect to the laser polarization in the laboratory frame. Electrons are mainly emitted at small angles and, due to the short nature of the pulse electron emission, are

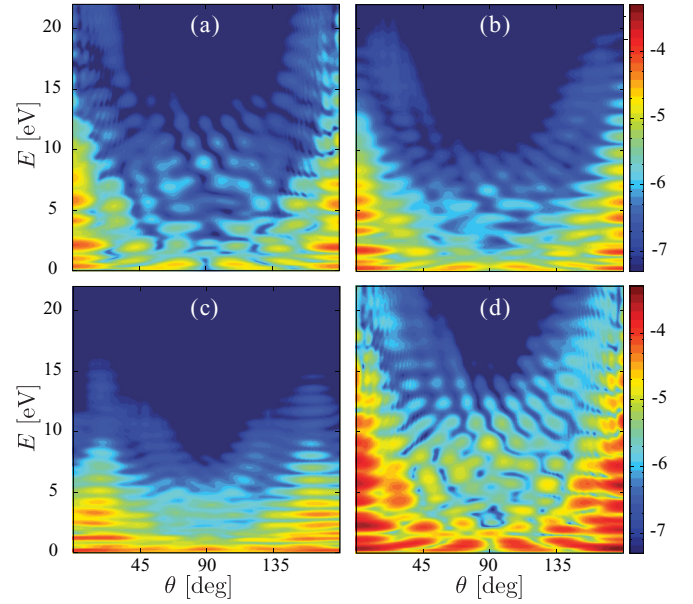


FIG. 10. (Color online) Photoelectron angle- and energy-resolved probability $P_{\theta_L}(E, \theta)$ (log scale) for aligned N_2 molecules and different laser polarization directions θ_L : (a) $\theta_L = 90^\circ$, (b) $\theta_L = 60^\circ$, (c) $\theta_L = 30^\circ$, and (d) $\theta_L = 0^\circ$. Here θ_L is the angle between the laser polarization direction and the molecular axis. Laser parameters are the same as in Fig. 9.

asymmetric along the laser polarization axis (at angles close to 0° and 180°).

We performed TDDFT calculations for different angles θ_L between the molecular axis and the laser polarization. The molecular geometry was set at the experimental equilibrium interatomic distance $R_0 = 2.074$ a.u. The Kohn-Sham wave functions were expanded in real space with spacing $\Delta r = 0.38$ a.u. in a simulation box of $R_A = 35$ a.u. The photoelectron spectra were calculated with FMM having $R_C = 25$ a.u., and padding factors $P = 1$ and $P_N = 4$.

In Fig. 10 the logarithmic ionization probability $P_{\theta_L}(E, \theta)$ is plotted as a function of energy E and angle θ measured from the laser polarization axis for different values of θ_L . As the molecular orientation decreases from $90^\circ \leq \theta_L \leq 30^\circ$ we observe an increasing suppression of the emission together with a shift of the maximum that moves away from the laser polarization axis. For $\theta_L = 0^\circ$ the emission is highly enhanced for all angles and peaked along the laser direction. The signature of multicenter emission interference has been predicted to be particularly marked when the laser polarization is perpendicular to the molecular axis [61,62] (i.e., $\theta_L = 90^\circ$). However, the lowest point in energy of such a pattern is predicted for $\theta = 90^\circ$ and $E = \pi^2 / 2R_0^2 \approx 31$ eV, way above the energy window of observable photoelectrons produced by our laser. A stronger and longer laser pulse would be required to extend the rescattering plateau toward higher energies and therefore to reveal the pattern [63].

In order to reproduce the experimental $\bar{P}(E, \theta)$, an average over all the possible molecular orientations should be performed. Due to the axial symmetry of the molecule we can restrict the average to $0 \leq \theta_L \leq 90^\circ$ and integrate all the

contributions with the proper probability weight [41]

$$\bar{P}(E, \theta) \propto \int_0^{90^\circ} d\theta_L \sin \theta_L P_{\theta_L}(E, \theta). \quad (23)$$

We evaluate Eq. (23) by discretizing the integral in a sum for $\theta_L = 0^\circ, 30^\circ, 60^\circ, 90^\circ$, and display the result in Fig. 9(b). Even in this crude approximation, and without taking into account focal averaging, the agreement with the experiment is satisfactory and compares favorably to the molecular strong-field approximation shown in Fig. 9(c). The agreement deteriorates for low energies where the importance of the Coulomb tail is enhanced as it is not fully accounted for due to limited dimensions of the simulation box. As a matter of fact, the agreement greatly increases for higher energies.

C. He-(I) PADs for carbon monoxide and benzene

In this section we deal with UV ($\omega = 0.78$ a.u.) angular resolved photoemission triggered by weak lasers. When the external field is weak, nonlinear effects can be discarded and first-order perturbation theory can be applied. In this situation, the momentum-resolved PES can be evaluated by Fermi's golden rule as

$$P(\mathbf{p}) \propto \sum_i |\langle \Psi_f | \mathbf{A}_0 \cdot \mathbf{p} | \Psi_i \rangle|^2 \delta(E_f - E_i - \omega), \quad (24)$$

where $|\Psi_i\rangle$ ($|\Psi_f\rangle$) is the initial (final) many-body wave function of the system and \mathbf{A}_0 is the laser polarization axis. The difficulty in evaluating Eq. (24) lies in the proper treatment of the final state, which in principle belongs to the continuum of the same Hamiltonian of $|\Psi_i\rangle$. In the simplest approach, it is approximated by a plane wave (PW). In this approximation the square root of the momentum-resolved PES is proportional to the sum of the Fourier transforms of the initial state wave functions $\tilde{\Psi}_i(\mathbf{p})$ corrected by a geometrical factor $|\mathbf{A}_0 \cdot \mathbf{p}|$,

$$\sqrt{P(\mathbf{p})} \propto \sum_i |\mathbf{A}_0 \cdot \mathbf{p}| |\tilde{\Psi}_i(\mathbf{p})|. \quad (25)$$

If photoemission peaks are well resolved in momentum, individual initial states can be selectively measured. In this case a correspondence between momentum-resolved PES and electronic states in reciprocal space can be established. The range of applicability of the PW approximation has been discussed in the literature [5]. It has been postulated that Eq. (25) should be valid for (i) π -conjugated planar molecules, (ii) constituted by light atoms (H, C, N, O), and for (iii) photoelectrons emerging with momentum \mathbf{p} almost parallel to the polarization axis.

Here we restrict ourselves to photoemission from the highest occupied molecular orbital (HOMO). In this case Eq. (25) becomes

$$\sqrt{P_H(\mathbf{p})} \propto |\mathbf{A}_0 \cdot \mathbf{p}| |\tilde{\Psi}_H(\mathbf{p})|, \quad (26)$$

with the subscript H indicating HOMO-related quantities. We compare *ab initio* TDDFT and PW PADs evaluated at fixed momentum $|\mathbf{p}_H| = \sqrt{2E_H}$ with $E_H = \omega - E_B$ being the kinetic energy of photoelectrons emitted from the HOMO and E_B its binding energy.

TDDFT numerical calculations are carried out on a grid with spacing $\Delta r = 0.28$ a.u. for benzene and $\Delta r = 0.38$ a.u.

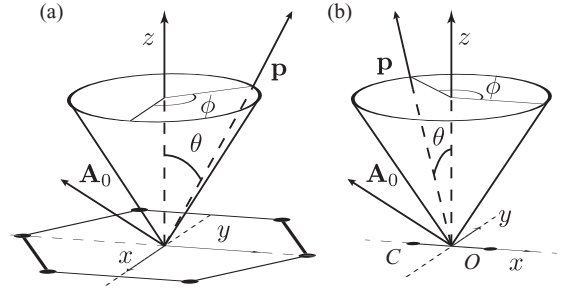


FIG. 11. Photoemission geometries for oriented (a) benzene and (b) CO molecules.

for CO, in a simulation box of $R_A = 30$ a.u. Photoelectron spectra are calculated using MM with $R_C = 20$ a.u. and padding factors $P = 1$, $P_N = 8$. A 40 cycles pulse with 8 cycle ramp at the He-(I) frequency $\omega = 0.78$ a.u. and intensity $I = 1 \times 10^8$ W/cm² is employed.

We begin presenting the case of benzene since it constitutes the smallest molecule meeting all the conditions for Eq. (26) to be valid. Results for molecules oriented according to Fig. 11(a), evaluated at $E_H = 0.363$ a.u., and two different laser polarizations $\mathbf{A}_0 = \hat{\mathbf{a}}_1, \hat{\mathbf{a}}_2$ with $\hat{\mathbf{a}}_1 = (1, 0, 0)$, $\hat{\mathbf{a}}_2 = 1/\sqrt{3} \times (1, 1, 1)$, are shown in Fig. 12. In the case where the laser is polarized along the x axis [see Fig. 12(b)], PAD presents a four lobes symmetry separated by three horizontal

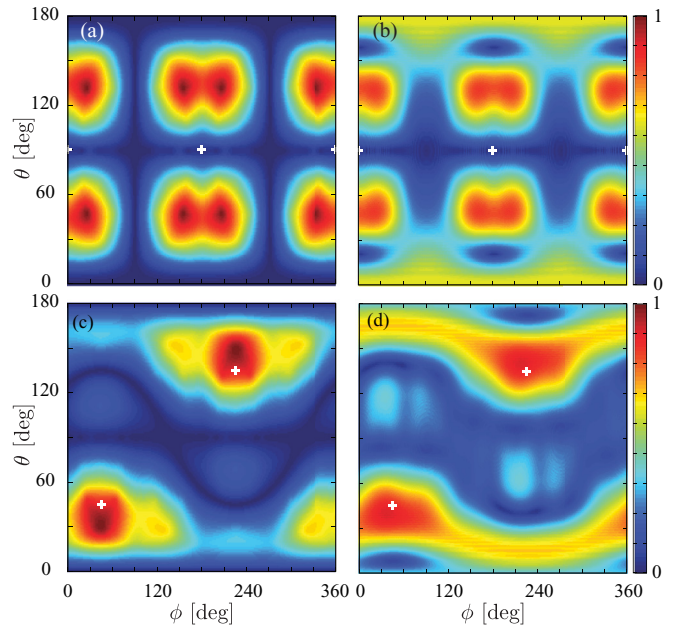


FIG. 12. (Color online) He-(I) PADs for aligned benzene molecules. We compare PADs from PW $|\mathbf{A}_0 \cdot \mathbf{p}| |\tilde{\Psi}_H(\mathbf{p})|$ (left column) and TDDFT $\sqrt{P_H(\mathbf{p})}$ (right column) on a sphere at constant kinetic energy $E_H = 0.363$ a.u. for different laser polarizations \mathbf{A}_0 (see text for details). Values on the sphere are normalized to unity. We used a 40 cycles (8 cycles ramp) UV trapezoidal laser pulse with $\lambda = 58$ nm ($\omega = 0.78$ a.u.), and intensity $I = 1 \times 10^8$ W/cm². In the top row $\mathbf{A}_0 = \hat{\mathbf{a}}_1 = (1, 0, 0)$, and in the bottom row $\mathbf{A}_0 = \hat{\mathbf{a}}_2 = 1/\sqrt{3} \times (1, 1, 1)$. White ticks indicate the intersection of the laser polarization axis with the sphere at constant kinetic energy E_H . The geometry of the photoemission process is indicated in Fig. 11(a).

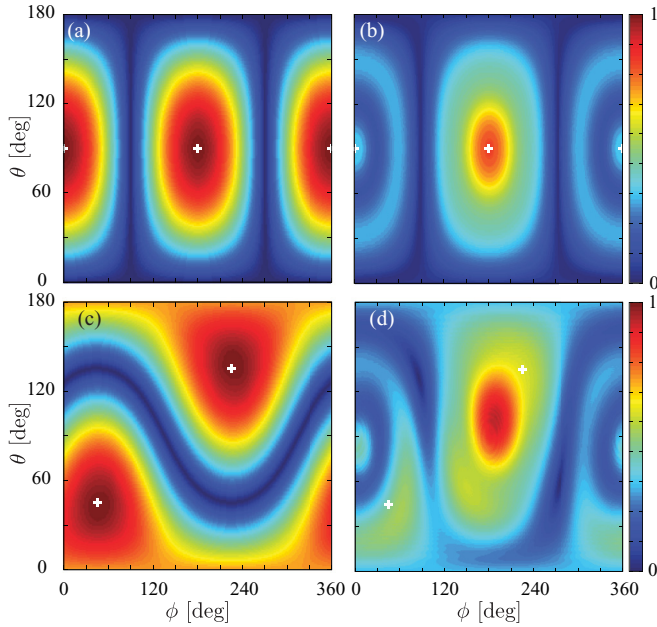


FIG. 13. (Color online) He-I PADs for aligned CO molecules. Panel ordering and laser parameters are the same as in Fig. 12. The molecule is oriented according to Fig. 11(b) and the photoelectron spectra were evaluated on a sphere at $E_h = 0.261$ a.u.

and two vertical nodal lines. This structure is reminiscent of the HOMO π symmetry with the nodal line at $\theta = 90^\circ$ corresponding to the nodes of the orbital on the x - y plane. Information on the orientation of the molecular plane could then be inferred from the inspection of this nodal line in the PAD. A similar feature can be observed also in the case of an off-plane polarization as shown in Fig. 12(d). In this case, however, the laser can also excite σ orbitals and the nodal line at $\theta = 90^\circ$ is partially washed out. The other nodal lines can be understood in term of zeros of the polarization factor $|\mathbf{A}_0 \cdot \mathbf{p}|$ and are thus purely geometrical. A PW approximation of the photoelectron distribution given by Eq. (26) qualitatively reproduce the *ab initio* results as shown in Figs. 12(a) and 12(d). According to condition (iii) a quantitative agreement is reached only for directions parallel to the polarization axis.

A different behavior is expected in the case of CO. Photoelectrons with kinetic energy of $E_H = 0.261$ a.u. are show in Fig. 13. In this case, condition (i) (i.e., π -conjugated molecule) is not fulfilled and a worse agreement between *ab initio* and PW calculations is expected. The quality of the agreement can be assessed by comparing the left and right columns of Fig. 13. Here, the weak angular variation of $|\tilde{\Psi}_H(\mathbf{p})|$ is completely masked by the polarization factor $|\mathbf{A}_0 \cdot \mathbf{p}|$ [cf. Figs. 13(a) and 13(c)]. For this reason no information on the molecular configuration can be recovered from a PW model.

The situation is qualitatively different for TDDFT as, in this case, single atom electron emitters are fully accounted for. Here the nodal pattern is mainly governed by the polarization factor, but, however, fingerprints of the molecule electronic configuration can be detected. For instance, when the laser is polarized along the molecular axis, an asymmetry of the photoemission maxima can be observed for directions parallel to $\hat{\mathbf{a}}_1$ [see Fig. 13(b)]. Here the global maximum is peaked

around $(\phi, \theta) = (180^\circ, 90^\circ)$ corresponding to the side of the carbon atom on the molecular axis [cf. Fig. 11(b)]. These features can be again understood in terms of the shape of the HOMO. For CO, in fact, the HOMO is a σ orbital with the electronic charge unevenly accumulated around the carbon atom. It is therefore natural to expect photoelectrons to be ejected mainly around the molecular axis and with higher probability from the side of the carbon atom. This asymmetry is therefore a property of the electronic configuration of the molecule and gives information about the molecular orientation itself. This behavior appears to be stable upon molecule rotation as can be observed in the case where the polarization is tilted with respect to the molecular axis [$\mathbf{A}_0 = \hat{\mathbf{a}}_1$; see Fig. 13(d)]. Even here the nodal structure is mainly dictated by the polarization factor.

IV. CONCLUSIONS

In this work we studied the problem of photoemission in finite systems with TDDFT. We presented a formal derivation of a photoelectron density functional from a phase-space approach to photoemission. Such a functional can be directly applied to other theories based on a single Slater determinant and the derivation could serve as a base for extensions to more refined models.

We proposed a mixed real- and momentum-space evolution scheme based on geometrical splitting. In its complete form it allows particles to seamlessly pass back and forth from a real-space description to a momentum-space description. The ordinary splitting scheme turns out to be a special case of this more general method. Furthermore, we illustrated applications of the method on four physical systems: hydrogen, molecular nitrogen, carbon monoxide, and benzene.

For hydrogen we presented a comparison of the different methods. We studied ATI peak formation in a one-dimensional model and ATI angular distributions for a three-dimensional case. The results turned out to be in good agreement with the literature. From the comparison, we derived a prescription to choose the best method based on a classification of the electron dynamics induced by the external field.

We investigated angular-resolved photoemission for randomly oriented N_2 molecules in a short intense IR laser pulse. We illustrated the results for four different molecular orientations with respect to the laser polarization. Owing to the symmetry of the problem we were able to combine the results to account for the random orientation. The spectrum for randomly oriented molecules is in good agreement with experimental measurements and is much better than the widely used strong-field approximations (with one active electron) [28].

We also studied UV angular-resolved photoelectron spectra for oriented carbon monoxide and benzene molecules. We presented numerical calculations for two different directions of the laser polarization and compared with the plane-wave approximation. We found that the plane-wave approximation provides a good description for benzene while failing for CO. Furthermore, we found evidence that the photoelectron angular distribution carries important information on molecular orientation.

The successful implementation of photoelectron density functional presented in this paper paves the road for interesting applications to many different systems for a wide range of laser parameters. To name a few, TDDFT PAD could provide a theoretical tool superior to the plane wave and the independent atomic center approximations to retrieve molecular adsorption orientation information from experiments. Attosecond pump probe experiments could be simulated *ab initio* accounting for many-body effects but with great computational advantage with respect to full many-body methods and better physical description than SAE pictures.

ACKNOWLEDGMENTS

Special thanks to Lorenzo Stella for many stimulating discussions and suggestions. We also wish to acknowledge useful discussions and comments from Stefan Kurth, Ilya Tokatly, Matteo Gatti, and Franck Lépine. Financial support was provided by Spanish (FIS2011-65702-C02-01 and PIB2010US-00652), ACI-Promociona (ACI2009-1036), Grupos Consolidados UPV/EHU del Gobierno Vasco (IT-319-07), and the European Research Council Advanced Grant DYnAmo (ERC-2010-AdG-Proposal No. 267374). Computational time was granted by i2basque and BSC Red Espanola de Supercomputacion. M.A.L.M. acknowledges support from the French ANR (ANR-08-CEXC8-008-01).

APPENDIX A: OVERLAP INTEGRALS

In this section we describe the details of the inclusion of the Kohn-Sham one-body density matrix (9) into Eq. (4). The momentum-resolved photoelectron probability is the sum over all the occupied orbitals of four overlap integrals γ ,

$$P(\mathbf{p}) = \sum_{i=1}^{\text{occ}} \gamma_{A,A,i}(\mathbf{p}) + \gamma_{A,B,i}(\mathbf{p}) + \gamma_{B,A,i}(\mathbf{p}) + \gamma_{B,B,i}(\mathbf{p}). \quad (\text{A1})$$

In order to simplify the notation we drop the orbital index i in the overlap integrals and indicate with $\mathbf{v} = v\hat{\mathbf{v}}$ the vector \mathbf{v} of modulus v and direction $\hat{\mathbf{v}}$. In addition, we will consider the simple case where the boundary surface between region A and B is a d -dimensional sphere of radius R_A .

We start by considering the mixed overlap,

$$\gamma_{AB}(\mathbf{p}) = \int_B d\mathbf{R} \int \frac{d\mathbf{s}}{(2\pi)^{\frac{d}{2}}} e^{i\mathbf{p}\cdot\mathbf{s}} \psi_A\left(\mathbf{R} + \frac{\mathbf{s}}{2}\right) \psi_B^*\left(\mathbf{R} - \frac{\mathbf{s}}{2}\right), \quad (\text{A2})$$

where the integration in B is for $R > R_A$ [cf. Fig. 1(a)]. It is convenient to work in the coordinates $\mathbf{v} = 2\mathbf{R}$ and $\mathbf{r} = \mathbf{R} + \mathbf{s}/2$, where the integral takes the form

$$\int_{v>2R_A} d\mathbf{v} \int \frac{d\mathbf{r}}{(2\pi)^{\frac{d}{2}}} e^{i\mathbf{p}\cdot(2\mathbf{r}-\mathbf{v})} \psi_A(\mathbf{r}) \psi_B^*(\mathbf{v}-\mathbf{r}). \quad (\text{A3})$$

We substitute ψ_B^* with its Fourier integral representation,

$$\psi_B^*(\mathbf{u}-\mathbf{r}) = \int \frac{d\mathbf{k}}{(2\pi)^{\frac{d}{2}}} e^{i\mathbf{k}\cdot(\mathbf{u}-\mathbf{r})} \tilde{\psi}_B^*(\mathbf{k}), \quad (\text{A4})$$

and after a few simple steps we obtain

$$\int \frac{d\mathbf{k}}{(2\pi)^{\frac{d}{2}}} \tilde{\psi}_A(-2\mathbf{p}-\mathbf{k}) \tilde{\psi}_B^*(\mathbf{k}) \int_{v>2R_A} d\mathbf{v} e^{-i(\mathbf{k}+\mathbf{p})\cdot\mathbf{v}}, \quad (\text{A5})$$

where we successfully disentangled the integration over \mathbf{v} in the second integral. The integral on $v > 2R_A$ can be rewritten as an integral over the whole space, which yields a d -dimensional Dirac delta, minus an integral on $v \leq 2R_A$:

$$\int_{v>2R_A} d\mathbf{v} e^{-i(\mathbf{k}+\mathbf{p})\cdot\mathbf{v}} = (2\pi)^d \delta(\mathbf{k}+\mathbf{p}) - (4\pi R_A)^{\frac{d}{2}} \frac{J_{d/2}(2R_A|\mathbf{k}+\mathbf{p}|)}{|\mathbf{k}+\mathbf{p}|^{\frac{d}{2}}}, \quad (\text{A6})$$

where $J_n(k)$ is a Bessel function of the first kind. The second term in Eq. (A6) is a function centered in $-\mathbf{p}$ and strongly peaked in the region $w = C_d/R_A$ with $C_1 = \pi$, $C_2 \approx 3.83$, and $C_3 \approx 4.49$ being the first zeros of the Bessel function $J_{d/2}(k)$. If the region w is small enough we can consider the integrand in \mathbf{k} of Eq. (A5) constant and factor out of the integrand $\tilde{\psi}_A(-2\mathbf{p}-\mathbf{k}) \tilde{\psi}_B^*(\mathbf{k})$ evaluated at $\mathbf{k} = -\mathbf{p}$. It is easy to see that

$$\int \frac{d\mathbf{k}}{(2\pi)^{\frac{d}{2}}} (2R_A)^{\frac{d}{2}} \frac{J_{d/2}(2R_A|\mathbf{k}+\mathbf{p}|)}{|\mathbf{k}+\mathbf{p}|^{\frac{d}{2}}} = 1 \quad (\text{A7})$$

and, by plugging Eq. (A6) in Eq. (A5), we have that $\gamma_{A,B}(\mathbf{p}) \approx 0$. By the same reasoning we should expect $\gamma_{B,A}(\mathbf{p}) \approx 0$.

We now turn to the terms containing the wave function on the same region. In (\mathbf{v}, \mathbf{r}) coordinates,

$$\gamma_{A,A}(\mathbf{p}) = \int_{v>2R_A} d\mathbf{v} \int \frac{d\mathbf{r}}{(2\pi)^{\frac{d}{2}}} e^{i\mathbf{p}\cdot(2\mathbf{r}-\mathbf{v})} \psi_A(\mathbf{r}) \psi_A^*(\mathbf{v}-\mathbf{r}). \quad (\text{A8})$$

The product of functions localized in A is not negligible only for $r < R_A$ and $|\mathbf{v}-\mathbf{r}| < R_A$. Since the integral is carried out for $v > 2R_A$ we can bound $|\mathbf{v}-\mathbf{r}|$ from below with $R_A|2\hat{\mathbf{v}}-\mathbf{r}/R_A| \geq R_A$. This leads to $R_A \leq |\mathbf{v}-\mathbf{r}| < R_A$, which is satisfied only on the boundary of A . Being a set of negligible measure we have $\gamma_{A,A}(\mathbf{p}) = 0$.

Once again, in (\mathbf{v}, \mathbf{r}) coordinates,

$$\gamma_{B,B}(\mathbf{p}) = \int_{v>2R_A} d\mathbf{v} \int \frac{d\mathbf{r}}{(2\pi)^{\frac{d}{2}}} e^{i\mathbf{p}\cdot(2\mathbf{r}-\mathbf{v})} \psi_B(\mathbf{r}) \psi_B^*(\mathbf{v}-\mathbf{r}) \quad (\text{A9})$$

can be written as

$$\gamma_{B,B}(\mathbf{p}) = |\psi_B(\mathbf{p})|^2 - \int_{v<2R_A} d\mathbf{v} \int \frac{d\mathbf{r}}{(2\pi)^{\frac{d}{2}}} e^{i\mathbf{p}\cdot(2\mathbf{r}-\mathbf{v})} \psi_B(\mathbf{r}) \psi_B^*(\mathbf{v}-\mathbf{r}), \quad (\text{A10})$$

where the first integration is in region A . Using the localization of ψ_B we see that the integral is nonzero only for $r > R_A$ and $|\mathbf{v}-\mathbf{r}| > R_A$. As the integration is for $v < 2R_A$ we have that $R_A \geq |\mathbf{v}-\mathbf{r}| > R_A$ and therefore the double integral in Eq. (A10) is zero.

APPENDIX B: NUMERICAL STABILITY AND FOURIER INTEGRALS

A real-space implementation of Eq. (15) involves the evaluation of several Fourier integrals. Such integrals are necessarily substituted by their discrete equivalent, and therefore discrete Fourier transforms (FT) and fast Fourier transforms (FFTs) are called into play. However, evolution methods based on the discrete FT naturally impose periodic boundary conditions. While this is not presenting any particular issue for MM where FT are only used to map real-space wave functions to momentum space, it is a source of numerical instability for FMM where the wave functions are reintroduced in the simulation box.

The problem is well illustrated by the following one-dimensional example. Imagine a wave packet freely propagating to an edge of the simulation box with a certain velocity. In MM, when passing through the buffer region, the packet is converted by discrete FT in momentum space and then analytically evolved as a free particle through the edge of the box. In FMM as the wave function evolves in momentum spaces it is also transformed back to real space to account for possible charge returns. In this case, instead of just disappearing from one edge, by virtue of the discrete FT periodic boundary conditions, the same wave packet will appear from the opposite side. It can be easily understood how such an undesirable event can create a feedback leading to an uncontrolled and unphysical buildup of the density.

This behavior can be controlled by the use of zero padding. As we know, the Fourier integrals in Eq. (15) involve functions that are, by construction, zero outside the buffer region C . We can therefore enlarge the integration domain (having radius R_A) by a padding factor P , set the integrand to zero in the extended points, obtaining the same result. As a consequence, a wave packet propagating toward a boundary edge will have to run an enlarged *virtual* box of radius $\tilde{R}_A = R_A(2P - 1)$ before emerging from the other side. In addition, the smallest momentum represented $\Delta\tilde{p} = 2\pi/PR_A = \Delta p/P$ in the

discretized $\tilde{\psi}_{B,i}(\mathbf{p}, t')$ is reduced by a factor $1/P$, while the highest momentum $p_{\max} = \pi/\Delta r$ remains unchanged. The price to pay here is an increased memory requirement by a factor P^d (where d is the dimension of the simulation box) and is too high for three-dimensional calculations.

A possible way to find a better scaling is offered by the use of nonuniform discrete Fourier transform and companion fast algorithm (NFFT) [64,65]. NFFT allow for the possibility to perform Fourier integrals on unstructured sampling points with, for fixed accuracy, the same arithmetical complexity as FFT. For a detailed description of the algorithm we refer to the literature [65]. The idea is to use the flexibility of NFFT to perform zero padding in a convenient way. Instead of allocating an enlarged box filled with zeros at equally spaced sample positions, we set only one point at $R_A P_N$ (here P_N is the NFFT padding factor) and evaluate the Fourier integral with NFFT. In this way we gain numerical stability for FMM as long as the wave functions are contained in a *virtual* box of $\tilde{R}_A = R_A(2P_N - 1)$ at the price of adding a number of points that scales as $d - 1$ with the dimension of the box. If N^d is the number of grid points in the simulation box, in order to perform zero padding with NFFT one needs to add only $2N^{d-1}$ points.

With this procedure, however, not only the smallest momentum $\Delta\tilde{p}$ is reduced by a factor $1/P_N$, but also the highest momentum $\tilde{p}_{\max} = (N/2 + 1)\Delta\tilde{p}$ is decreased by the same amount. This turns out to be the limiting factor in the use of NFFT to preserve numerical stability with FMM as the enlargement factor P_N has an upper bound that depends on the escaping electron dynamics. In fact, when we evaluate the back-action term Eq. (16b), we assume $\tilde{\psi}_{B,i}(\mathbf{p}, t')$ to be localized in momentum and, in order to preserve numerical consistency, P_N must be limited by the highest momentum contained in $\tilde{\psi}_{B,i}$. A combination of ordinary padding and NFFT padding helps to balance the tradeoff between memory occupancy and numerical stability.

Finally, in MM zero padding can be used to increase resolution in momentum.

-
- [1] A. Ellis, M. Fehér, and T. Wright, *Electronic and Photoelectron Spectroscopy: Fundamentals and Case Studies* (Cambridge University Press, Cambridge, UK, 2005).
 - [2] G. Wu, P. Hockett, and A. Stolow, *Phys. Chem. Chem. Phys.* **13**, 18447 (2011).
 - [3] T. Brabec and F. Krausz, *Rev. Mod. Phys.* **72**, 545 (2000).
 - [4] F. Krausz, *Rev. Mod. Phys.* **81**, 163 (2009).
 - [5] P. Puschnig, S. Berkebile, A. J. Fleming, G. Koller, K. Emtsev, T. Seyller, J. D. Riley, C. Ambrosch-Draxl, F. P. Netzer, and M. G. Ramsey, *Science* **326**, 702 (2009).
 - [6] S. Kera, S. Tanaka, H. Yamane, D. Yoshimura, K. K. Okudaira, K. Seki, and N. Ueno, *Chem. Phys.* **325**, 113 (2006).
 - [7] M. Schultze, M. Fiess, N. Karpowicz, J. Gagnon, M. Korbman, M. Hofstetter, S. Neppl, A. L. Cavalieri, Y. Komninos, T. Mercouris *et al.*, *Science* **328**, 1658 (2010).
 - [8] T. Remetter, P. Johnsson, J. Mauritsson, K. Varjú, Y. Ni, F. Lepine, E. Gustafsson, M. Kling, J. Khan, R. López-Martens *et al.*, *Nature Phys.* **2**, 323 (2006).
 - [9] M. Meckel, D. Comtois, D. Zeidler, A. Staudte, D. Pavicic, H. C. Bandulet, H. Pépin, J. C. Kieffer, R. Dorner, D. M. Villeneuve *et al.*, *Science* **320**, 1478 (2008).
 - [10] Y. Huismans, A. Rouzee, A. Gijsbertsen, J. H. Jungmann, A. S. Smolkowska, P. S. W. M. Logman, F. Lepine, C. Cauchy, S. Zamith, T. Marchenko *et al.*, *Science* **331**, 61 (2011).
 - [11] P. B. Corkum, *Phys. Rev. Lett.* **71**, 1994 (1993).
 - [12] M. Lein, E. K. U. Gross, and V. Engel, *Phys. Rev. A* **64**, 023406 (2001).
 - [13] R. Pazourek, J. Feist, S. Nagele, and J. Burgdörfer, *Phys. Rev. Lett.* **108**, 163001 (2012).
 - [14] K. L. Ishikawa and K. Ueda, *Phys. Rev. Lett.* **108**, 033003 (2012).
 - [15] K. J. Schafer and K. C. Kulander, *Phys. Rev. A* **42**, 5794 (1990).
 - [16] S. Chelkowski, C. Foisy, and A. D. Bandrauk, *Phys. Rev. A* **57**, 1176 (1998).
 - [17] R. Grobe, S. Haan, and J. Eberly, *Comput. Phys. Commun.* **117**, 200 (1999).

- [18] Z. Chen, T. Morishita, A.-T. Le, M. Wickenhauser, X. M. Tong, and C. D. Lin, *Phys. Rev. A* **74**, 053405 (2006).
- [19] X. M. Tong, K. Hino, and N. Toshima, *Phys. Rev. A* **74**, 031405 (2006).
- [20] X. Tong, K. Hino, N. Toshima, and J. Burgdörfer, *J. Phys.: Conf. Ser.* **88**, 012047 (2007).
- [21] M. Awasthi, Y. V. Vanne, A. Saenz, A. Castro, and P. Decleva, *Phys. Rev. A* **77**, 063403 (2008).
- [22] S. Petretti, Y. V. Vanne, A. Saenz, A. Castro, and P. Decleva, *Phys. Rev. Lett.* **104**, 223001 (2010).
- [23] I. A. Burenkov, A. M. Popov, O. V. Tikhonova, and E. A. Volkova, *Laser Phys. Lett.* **7**, 409 (2010).
- [24] Z. Zhou and S.-I. Chu, *Phys. Rev. A* **83**, 013405 (2011).
- [25] L. Tao and A. Scrinzi, *New J. Phys.* **14**, 013021 (2012).
- [26] F. Catoire and H. Bachau, *Phys. Rev. A* **85**, 023422 (2012).
- [27] W. D. Grobman, *Phys. Rev. B* **17**, 4573 (1978).
- [28] A. Gazibegovic-Busuladzic, E. Hasovic, M. Busuladzic, D. B. Milosevic, F. Kelkensberg, W. K. Siu, M. J. J. Vrakking, F. Lepine, G. Sansone, M. Nisoli, I. Znakovskaya, and M. F. Kling, *Phys. Rev. A* **84**, 043426 (2011).
- [29] M. Lewenstein, K. C. Kulander, K. J. Schafer, and P. H. Bucksbaum, *Phys. Rev. A* **51**, 1495 (1995).
- [30] G. G. Paulus, W. Becker, W. Nicklich, and H. Walther, *J. Phys. B: At. Mol. Opt. Phys.* **27**, L703 (1999).
- [31] E. Runge and E. K. U. Gross, *Phys. Rev. Lett.* **52**, 997 (1984).
- [32] M. A. L. Marques, N. T. Maitra, F. Nogueira, E. K. U. Gross, and A. Rubio, *Fundamentals of Time-Dependent Density Functional Theory* (Springer-Verlag, Berlin, 2011).
- [33] X. Chu and S.-I. Chu, *Phys. Rev. A* **70**, 061402 (2004).
- [34] D. A. Telnov and S.-I. Chu, *Phys. Rev. A* **79**, 041401 (2009).
- [35] S.-K. Son and S.-I. Chu, *Phys. Rev. A* **80**, 011403 (2009).
- [36] S.-K. Son and S.-I. Chu, *Chem. Phys.* **366**, 91 (2009).
- [37] J. L. Hansen, L. Holmegaard, J. H. Nielsen, H. Stapelfeldt, D. Dimitrovski, and L. B. Madsen, *J. Phys. B: At. Mol. Opt. Phys.* **45**, 015101 (2011).
- [38] A. Pohl, P.-G. Reinhard, and E. Suraud, *Phys. Rev. Lett.* **84**, 5090 (2000).
- [39] A. Pohl, P.-G. Reinhard, and E. Suraud, *Phys. Rev. A* **70**, 023202 (2004).
- [40] P. Wopperer, B. Faber, P. Dinh, P.-G. Reinhard, and E. Suraud, *Phys. Lett. A* **375**, 39 (2010).
- [41] P. Wopperer, B. Faber, P. M. Dinh, P.-G. Reinhard, and E. Suraud, *Phys. Rev. A* **82**, 063416 (2010).
- [42] A. Castro, H. Appel, M. Oliveira, C. A. Rozzi, X. Andrade, F. Lorenzen, M. A. L. Marques, E. K. U. Gross, and A. Rubio, *Phys. Status Solidi B* **243**, 2465 (2006).
- [43] X. Andrade, J. Alberdi-Rodriguez, D. A. Strubbe, M. J. Oliveira, F. Nogueira, A. Castro, J. Muguerza, A. Arruabarrena, S. G. Louie, A. Aspuru-Guzik *et al.*, *J. Phys.: Condens. Matter* **24**, 233202 (2012).
- [44] D. A. Telnov and S.-I. Chu, *Phys. Rev. A* **79**, 043421 (2009).
- [45] N. Helbig, J. I. Fuks, M. Casula, M. J. Verstraete, M. A. L. Marques, I. V. Tokatly, and A. Rubio, *Phys. Rev. A* **83**, 032503 (2011).
- [46] M. Lewenstein, P. Balcou, M. Y. Ivanov, A. L'Huillier, and P. B. Corkum, *Phys. Rev. A* **49**, 2117 (1994).
- [47] D. Varsano, M. A. L. Marques, and A. Rubio, *Comput. Mater. Sci.* **30**, 110 (2004).
- [48] A. Castro, M. A. L. Marques, and A. Rubio, *J. Chem. Phys.* **121**, 3425 (2004).
- [49] A. N. Grum-Grzhimailo, B. Abeln, K. Bartschat, D. Weflen, and T. Urness, *Phys. Rev. A* **81**, 043408 (2010).
- [50] I. A. Ivanov, *Phys. Rev. A* **83**, 023421 (2011).
- [51] M. G. Pullen, W. C. Wallace, D. E. Laban, A. J. Palmer, G. F. Hanne, A. N. Grum-Grzhimailo, B. Abeln, K. Bartschat, D. Weflen, I. Ivanov *et al.*, *Opt. Lett.* **36**, 3660 (2011).
- [52] J. Zheng, E. Qiu, Y. Yang, and Q. Lin, *Phys. Rev. A* **85**, 013417 (2012).
- [53] R. van Leeuwen and E. J. Baerends, *Phys. Rev. A* **49**, 2421 (1994).
- [54] U. Schwengelbeck and F. H. M. Faisal, *Phys. Rev. A* **50**, 632 (1994).
- [55] A. Kästner, F. Grossmann, R. Schmidt, and J.-M. Rost, *Phys. Rev. A* **81**, 023414 (2010).
- [56] A. Gordon, R. Santra, and F. X. Kärtner, *Phys. Rev. A* **72**, 063411 (2005).
- [57] R. Kosloff and D. Kosloff, *J. Comput. Phys.* **63**, 363 (1986).
- [58] C. Jhala, I. Dreisigacker, and M. Lein, *Phys. Rev. A* **82**, 063415 (2010).
- [59] D. G. Arbó, J. E. Miraglia, M. S. Gravielle, K. Schiessl, E. Persson, and J. Burgdörfer, *Phys. Rev. A* **77**, 013401 (2008).
- [60] D. G. Arbó, S. Yoshida, E. Persson, K. I. Dimitriou, and J. Burgdörfer, *Phys. Rev. Lett.* **96**, 143003 (2006).
- [61] M. Busuladzic, A. Gazibegovic-Busuladzic, D. B. Milosevic, and W. Becker, *Phys. Rev. A* **78**, 033412 (2008).
- [62] M. Busuladzic, A. Gazibegovic-Busuladzic, D. B. Milosevic, and W. Becker, *Phys. Rev. Lett.* **100**, 203003 (2008).
- [63] M. Okunishi, R. Itaya, K. Shimada, G. Prümper, K. Ueda, M. Busuladzic, A. Gazibegovic-Busuladzic, D. B. Milosevic, and W. Becker, *Phys. Rev. Lett.* **103**, 043001 (2009).
- [64] S. Kunis and D. Potts, *Sampl. Theory Signal Image Process.* **7**, 77 (2008).
- [65] J. Keiner, S. Kunis, and D. Potts, *ACM Trans. Math. Software* **36**, 1 (2009).